Design of a Dispersive 1064 nm Fiber Probe Raman Imaging Spectrometer and Its Application to Human Bladder Resectates

Juan David Munoz-Bolanos , Tanveer Ahmed Shaik , Arkadiusz Miernik , Juergen Popp , Christoph Krafft *

Posted Date: 15 April 2024

doi: 10.20944/preprints202404.0864.v1

Keywords: bladder tumor; Raman imaging; 1064 nm; cluster analysis; Python toolbox

 doi:10.20944/preprints202404.0864.v1

Article

Design of a Dispersive 1064 nm Fiber Probe Raman Imaging Spectrometer and Its Application to Human Bladder Resectates

Juan David Muñoz-Bolaños [1], Tanveer Ahmed Shaik [1], Arkadiusz Miernik [2], Jürgen Popp [1,3] and Christoph Krafft [1,*]

[1] Leibniz Institute of Photonic Technology, Member of Leibniz Health Technologies and Member of the Leibniz Centre for Photonics in Infection Research, 07745 Jena, Germany
[2] University of Freiburg – Medical Center, Faculty of Medicine, Department of Urology, 79106 Freiburg, Germany
[3] Institute of Physical Chemistry and Abbe Center of Photonics, Friedrich Schiller Jena University, Member of the Leibniz Centre for Photonics in Infection Research, 07743 Jena, Germany
* Correspondence: Christoph.krafft@leibniz-ipht.de

Abstract: This study introduces a compact Raman spectrometer with a 1064 nm excitation laser coupled with a fiber probe and an inexpensive motorized stage, offering a promising alternative to widely used Raman imaging instruments with 785 nm excitation lasers. The benefits of 1064 nm excitation for biomedical applications include further suppression of fluorescence background and deeper tissue penetration. The performance of the 1064 nm instrument in detecting cancer in human bladder resectates is demonstrated. Raman images with 1064 nm excitation were collected ex vivo from 10 human tumor and non-tumor bladder specimens and the results are compared to previously published Raman images with 785 nm excitation. K-Means cluster (KMC) analysis is used after pre-processing to identify Raman signatures of control, tumor, necrosis, and lipid-rich tissues. Hierarchical cluster analysis (HCA) groups the KMC centroids of all specimens as input. The tools for data processing and hyperspectral analysis were compiled in an open source Python library called SpectraMap (SpMap). In conclusion, the 1064 nm Raman system can differentiate between tumor and non-tumor bladder tissues in a similar way to 785 nm Raman spectroscopy. These findings hold promise for future clinical hyperspectral Raman imaging, in particular for specimens with intense fluorescence background, e.g. kidney stones that are discussed as another widespread urological application.

Keywords: bladder tumor; Raman imaging; 1064 nm; cluster analysis; Python toolbox

1. Introduction

Optical and spectral technologies offer many opportunities in intraoperative histopathology. Among the techniques that are already approved or close to being applied in standard clinical practice for *in vivo* and *ex vivo* monitoring are Raman-based methods [1]. Raman spectroscopy probes inherent molecular vibrations without markers by inelastic scattering of monochromatic laser light. The general advantages are no or minimal sample preparation, no need for extrinsic markers, and high specificity of the spectrum of Raman-active vibrations. The main limitation of spontaneous Raman spectroscopy as a biomedical tool is due to the weak scattering cross sections of biomolecules and fluorescence emission of chromophores that overlap or obscure the Raman signals even in trace amounts. Several Raman variants were developed in the past decade to overcome this limitation including (i) coherent Raman scattering [2,3], (ii) time-gated Raman scattering [4] and (iii) shifted excitation Raman difference spectroscopy [5,6] that are all experimentally complex, (iv) surface enhanced Raman scattering [7,8] which requires complex preparation protocols involving nanostructured surfaces or particles, and (v) data processing procedures [9] that require expert

 doi:10.20944/preprints202404.0864.v1

knowledge in data science. An alternative approach that was developed more than two decades ago is spontaneous Raman spectroscopy with 1064 nm laser excitation. As this excitation wavelength is not absorbed by most chromophores, the acquired Raman spectra are minimally affected by fluorescence background. A first technical realization used the Fourier transformation (FT) principle with a liquid nitrogen cooled germanium-based detector for registration of Raman spectra [10]. With the advent of dispersive spectrometers with holographic transmissive gratings and indium gallium arsenide (InGaAs) based array detectors, a new generation of versatile Raman instruments were developed that are compact, less expensive and more sensitive than FT-Raman systems[11,12]. In this work, a laser and spectrometer for 1064 nm Raman spectroscopy are coupled with a fiber-optic Raman probe, an inexpensive motorized stage and a digital camera. As a first biomedical application, Raman images are collected from bladder tissue specimens for tumor identification.

Bladder cancer is the 10th most frequently diagnosed cancer worldwide (source: World Cancer Research Fund International[13]). Cystoscopy is the standard diagnostic method followed by excision of surgical biopsies and pathological inspection [14]. Raman spectroscopic-based techniques have been suggested as a complementary diagnostic tool to assess bladder tissues *ex vivo* in thin sections or biopsies, and *in vivo* during cystoscopy. Raman papers in the context of bladder cancer between 2005 and 2022 have recently been summarized [15]. Of particular relevance for the current work was the characterization of bladder tissue using probe-based Raman spectroscopy[16]. As most Raman spectra in this study were affected by an intense background, a data processing workflow was presented to suppress the background. Subsequently, machine learning models distinguished tumor from non-tumor with sensitivity and specificity of 92% and 93%, respectively, and low-grade from high-grade tumor tissues with sensitivity and specificity of 85% and 83%, respectively. A more recent work demonstrated the combination of a 2D spectrogram along with a convolutional neural network for the diagnosis of bladder cancer with an even higher accuracy of 99.2% [17]. Here, upscaling techniques were used to transform 1D Raman spectral data into a variety of 2D spectrograms. In addition, a weighted feature fusion network was constructed which was employed to evaluate multiple spectrograms. A translational approach introduced the combined use of *in vivo* Raman spectroscopy and *in vivo* cryoablation to detect and remove residual bladder tumor during transurethral resection of bladder tumor (TURBT) [18]. First, reference Raman spectra were collected from a group of 74 bladder cancer patients and a machine learning model was trained for classification. Then, an independent group of 26 patients accepted traditional TURBT, whereas another group of 27 patients accepted TURBT followed by Raman scanning and cryoablation if Raman detected existence of residual tumor. Interestingly, 2 in 27 patients had cancer recurrence in Raman-Cryoablation group, while 8 in 26 patients had cancer recurrence in traditional TURBT group during follow-up. This shows how the combined use of Raman and cryoablation can serve as adjuvant therapy to improve therapeutic effects and reduce recurrence rates.

The current work applies for the first time an in-house developed dispersive 1064 nm Raman instrument to collect Raman images from bladder tissue. The reduced background is expected to simplify the data processing and to contribute to improved tumor identification. The sample cohort consists of non-tumor and tumor specimens that were prepared from ten human bladder resectates. The samples were already studied by 785 nm Raman microscopic imaging [15] and the previous results are compared with the new results. As most bladder specimens showed an unusual low background in the 785 nm Raman study, the Raman analysis of four kidney stones were included in the discussion section. Two of them did not give usable Raman spectra at 785 nm excitation, whereas high quality spectra were acquired with the 1064 nm Raman system.

2. Materials and Methods

2.1. Dispersive Raman Instrument with 1064 nm Excitation Laser

A schematic of the dispersive Raman instrument with 1064 nm excitation laser is depicted in Figure 1a. The compact spectrometer (Wasatch Photonics, USA) offered a spectral range of 250-1850 cm^{-1} using a holographic transmissive grating. The spectral resolution was 10 cm^{-1} at a slit size of 50 µm. The spectrometer featured a 512-pixel InGaAs array detector (Hamamatsu G9214-512S, pixel size

 doi:10.20944/preprints202404.0864.v1

25×500 nm) which was thermoelectrically cooled to -15°C. A 1064 nm laser (Innovative Photonics Solution, USA) was coupled via a 105 µm multimode fiber to a Raman probe with a focusing lens of numerical aperture 0.3 (Wasatch Photonics, USA). The Raman probe focused the laser to a spot diameter of roughly 200 µm. A collection fiber with 600 µm core diameter guided the Raman scattered signal to the spectrometer. Raman images were acquired using an inexpensive three-dimensional stage (SainSmart Genmitsu CNC 3018-PRO, China). A USB-coupled full HD digital microscope camera (Facamword, USA) was installed next to the fiber probe, and the offset between the microscope and Raman probe was calibrated to define the region-of-interest. In-house LabVIEW (National Instruments, USA) routines were developed to control the components and spectra acquisition. Raman images were acquired from bladder tissue samples with an exposure time of 10 s, laser power of 450 mW, and 400 to 500 µm step size.

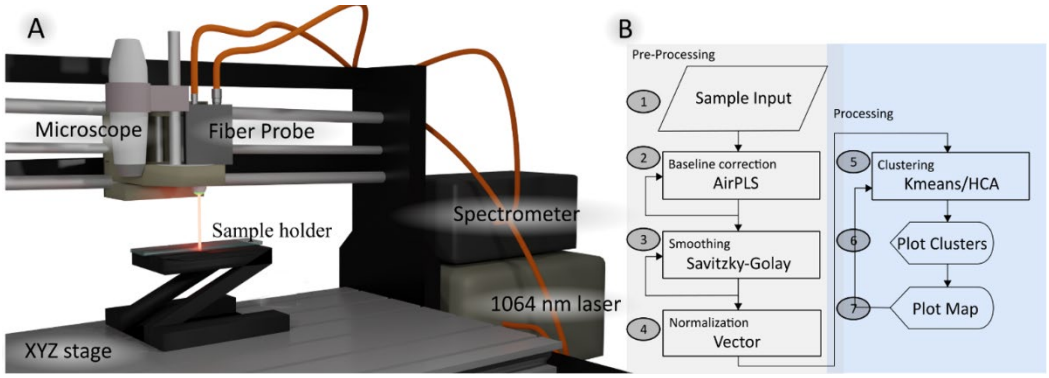

Figure 1. Dispersive Raman instrument with 1064 excitation laser (A) with fiber probe, microscope and motorized stage and (B) hyperspectral processing algorithm provided by SpMap.

2.2. Data Analysis

The Python package SpMap performed all spectral processing [19]. The data processing workflow is shown in Figure 1B. SpMap provides several pre-processing tools such as dark noise subtraction, wavelength and intensity calibration, cosmic ray correction and filtering of spectra below an intensity threshold. To suppress detector and probe background noise, a dark spectrum (laser off) and probe background (laser on) without sample were collected. Then, the fingerprint region from 500 to 1800 cm^{-1} was selected. An advanced airPLS baseline correction [20] was applied to remove the remaining tissue and microscope system backgrounds. Finally, all spectra were smoothed with a Savitzky-Golay filter [21] and vector normalized.

After preprocessing, the first step involved the use of k-means cluster analysis (KMC) in the spectral range 600-1800 cm^{-1} to identify main spectral signatures in each sample, such as control, tumor, and necrosis and lipid-rich tissues. KMC was also employed to reduce the size of data to a few clusters and increase the signal to noise ratios because each cluster centroid represents the mean of the cluster. These cluster centroids were then labeled based on the sample origin, i.e., whether they originate from a non-tumor or a tumor specimen. Hierarchical cluster analysis (HCA) was then performed in the spectral range 800-1150 cm^{-1} to arrange the KMC centroids found in the bladder tissue into the four categories, thereby reducing the computational cost. As the distance matrix in HCA can become large and calculation of the dendrogram can become time-consuming for large data sets, this strategy has been applied before, e.g. in the context of FTIR imaging [22].

2.3. Study Population

The study used both non-tumor and tumor samples from ten human bladder resections obtained from the tissue bank of the Comprehensive Cancer Centre Freiburg (Germany). The samples were shipped on dry ice to Jena and stored at -80°C until 785 nm Raman experiments. After finishing 785 nm data collection, the samples were stored again in the -80°C freezer until 1064 nm Raman experiments. The size of each sample was approximately 10×10 mm^2 and measurements were performed in a closed sample chamber without any sample preparation as described previously[15].

 doi:10.20944/preprints202404.0864.v1

3. Results

3.1. K-Means Cluster Analysis of Tumor 3 and Control 5 Specimens

Figure 2 shows photomicrographs and KMC membership maps of control bladder sample 5 (A, B) and tumor bladder sample 3 (C, D). Figure 2E shows cluster centroid spectra in the fingerprint region (600-1800 cm^{-1}) of control bladder, lipid-rich tissue, and bladder tumor. The spectral results followed the processing workflow shown in Figure 1B. Lipid-rich tissue can be found both inside and around the tissue sample (Figure 2B). The control and tumor tissue are most abundant throughout the sample (Figure 2B and 2D). Spectra of lipid-rich tissue has strong signatures at 1300 and 1447 cm^{-1}, that are characteristic of CH_2 bending vibrations, and at 1272 and 1663 cm^{-1}, that are characteristic of C=CH and C=C vibrations, respectively, in unsaturated lipids. Further spectral contributions in lipid-rich tissues are due to phosphate groups at 1082 cm^{-1} and C=O groups at 1746 cm^{-1} typical for phospholipids. The tumor and control signatures show bands at 1006, 1253-1312, and 1656 cm^{-1}, which are characteristic of phenylalanine, amide III and amide I vibrations, respectively. Further bands at 861 and 935 cm^{-1} are assigned to collagen triple helices of fibrous proteins that are more intense in control than in tumor bladder. The bands around 1660 cm^{-1} are broader for control and tumor bladder than for lipids because the amide I band which is a marker for protein secondary structures has a larger width than the C=C band of lipids. More detailed band assignments are given in the supplementary material of Krafft et al. [15].

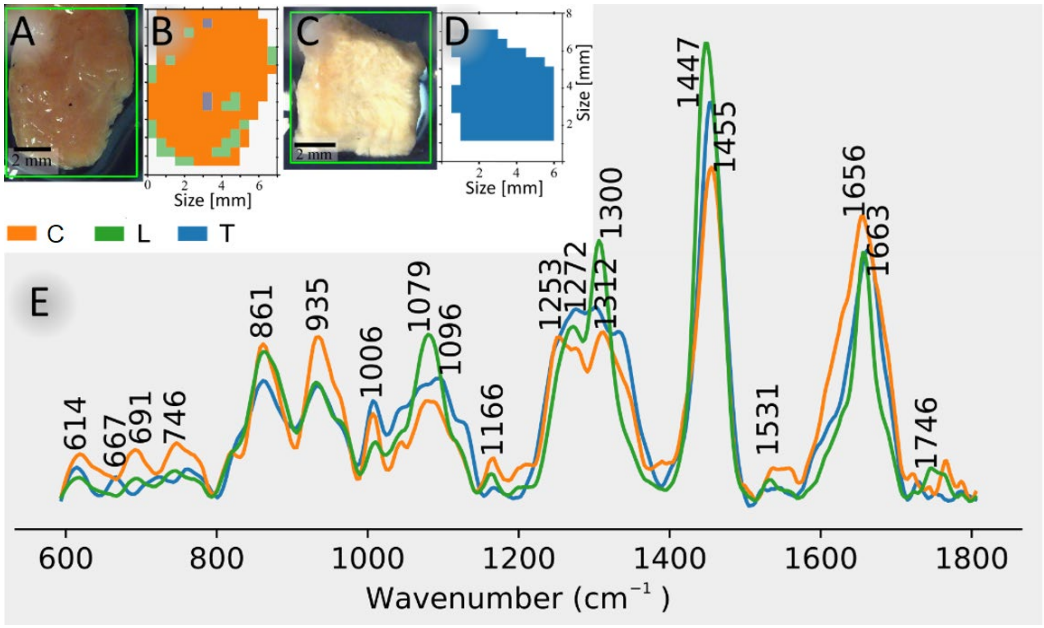

Figure 2. K-means cluster analysis of Raman images: photomicrographs and cluster membership maps of control bladder sample 5 (A, B) and tumor bladder sample 3 (C, D), and cluster centroid spectra of control (C), tumor (T), and lipid-rich (L) tissues (E).

3.2. Overview of the Clustering Results of the Specimens

Table 1 summarizes the results of an HCA for which the KMC centroids of non-tumor and tumor samples served as input. The dendrogram of the HCA in Figure 3 arranges the centroids of 23 clusters into four groups, namely lipids L, necrosis N, tumor T and control C. Non-tumor and tumor samples 8 and tumor sample 4 did not give usable data because of carbon-like appearance probably due to cauterization during surgery. It is evident from Table 1 and Figure 3, that non-tumor specimens contain beside control and lipid-rich tissue also tumor in 1 and 2, and vice versa tumor specimens contain beside tumor and necrosis also control tissue in 7 and 10. This is consistent with the previous study and will be discussed in Section 4.

Preprints.org (www.preprints.org) | NOT PEER-REVIEWED | Posted: 15 April 2024 doi:10.20944/preprints202404.0864.v1

Table 1. Assignment of cluster membership of centroid Raman spectra: control (C), necrosis (N), tumor (T) and lipid-rich tissue (L). Shaded entries are from previous work[15].

Specimen	1	2	3	4	5	6	7	8	9	10
Non-tumor	L, T	L, T	L, N	C	L, C	L. C	C	–	L, C	C
Non-tumor	L, T	T	L, T	L, C	L, C	L, C	C	C	L, C	L, C
Tumor	N	T	T	–	N	T	C	–	T	C
Tumor	N	T, L, N	T	T, L	T, L, N	T	T	–	T, L	L, N

The dendrogram arranges lipid-rich tissues of non-tumor specimens 1, 2, 3, 5, 6, and 9 in a well-separated group. Necrotic tissues are identified in non-tumor specimen 3 and tumor specimens 1 and 5. Tumor tissues are found in four tumor and two non-tumor specimens, and control tissue in six non-tumor and two tumor specimens.

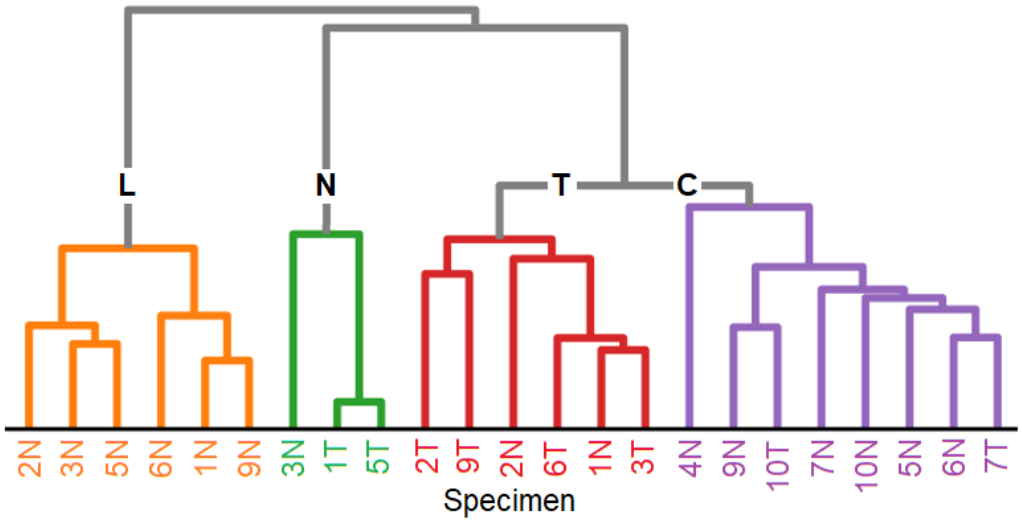

Figure 3. Dendrogram of hierarchical cluster analysis with k-means cluster centroids of Raman spectra as input: tumor (red), lipid (orange), necrosis (green), and control (purple) in the spectral region 800-1150 cm^{-1}. The samples are labeled as non-tumor (N) and tumor (T) according to Table 1.

3.3. Variations of Raman Spectra of Tumor and Control Tissue

Figure 4 compares the four tumor-assigned clusters in tumor specimens and six control-assigned clusters in non-tumor specimens. Control tissues tend to show more intense collagen bands near 850 and 935 cm^{-1} relative to the phenylalanine band at 1006 cm^{-1} than tumor tissue. Therefore, HCA was performed in the spectral range 800-1150 cm^{-1}. Unspecific variations were evident for band positions and intensities in the spectral range from 1150 to 1400 cm^{-1}. Similarly, main bands near 1450 and 1660 cm^{-1} did not change significantly and the observed changes did not improve the separation of tissue classes.

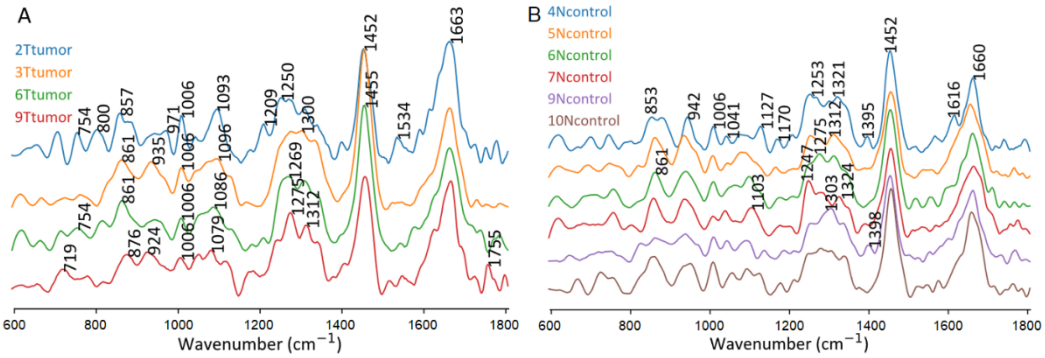

 doi:10.20944/preprints202404.0864.v1

Figure 4. Centroid Raman spectra of tumor-assigned clusters in tumor specimens (A) and control-assigned clusters in control specimens (B).

4. Discussion

Although the experimental parameters and data processing differed between 1064 nm and 785 nm Raman instruments, the main results agree well. The results at 785 nm excitation were included in Table 1. Lipid and control tissues were detected in non-tumor specimen 5, and tumor was detected in tumor specimen 3 both in this work using the 1064 nm Raman probe system and in the previous work using a 785 nm Raman microscope [15]. Whereas the agreement between both instruments is also very well for non-tumor specimens, more discrepancies occur for tumor specimens. Relevant difference in non-tumor 3 is the detection of necrosis at 1064 nm excitation and tumor at 785 nm. Relevant differences (i) in tumor 5 is the detection of necrosis at 1064 nm excitation and tumor, lipid, necrosis at 785 nm, and (ii) in tumor 7 is the detection of control at 1064 nm and tumor at 785 nm. Possible explanations are different orientations and heterogeneities because the sample has been put back to the vial after 785 nm experiments, frozen, thawed and mounted again into the holder for the 1064 nm experiments. During intraoperative frozen section analysis, the sample orientation in the resection area is marked with ink spots to avoid ambiguities. However, the spectral contributions of the ink may disturb the Raman results.

There is a tendency that more tissue types are identified at 785 nm excitation. For simplicity in Table 1, epithelial tissue, the plastic and pigment particles were not included that were detected at 785 nm excitation, but not at 1064 nm excitation. Possible explanations are the better spectral resolution of 4 cm^{-1} at 785 nm (instead of 10 cm^{-1} here), better lateral resolution at a step size of 250 µm (instead of 400 to 500 µm here), and the vertex component analysis (VCA) algorithm. The superior discriminatory power of VCA was already demonstrated to visualize single cell nuclei Raman images of lung tissue [23]. KMC that was applied here failed to resolve cell nuclei in the same data sets.

The dendrograms of the HCA show for 1064 and 785 nm data that tumor forms a separate group, and lipid-rich tissues are well separated from necrosis, tumor and control. Necrosis was arranged between tumor and lipids here, whereas necrosis overlaps with control at 785 nm excitation. This can be explained by the selected spectral range from 800 to 1150 cm^{-1} here and from 800 to 1380 cm^{-1} in reference [15]. Tumor tissue is characterized by lower spectral contributions of collagenous proteins relative to non-collagenous proteins which is detectable in both spectral ranges. A smaller spectral range was chosen due to unspecific variations that will be further studied in upcoming work.

In the urological context, Raman-based techniques also offer potential applications in kidney diseases[24]. Raman spectroscopy of urinary calculi was already reviewed in 1997[25], and the progress for analysis and classification of kidney stones has recently been reported[26]. Raman spectra were used to identify cystine-type kidney stones[27], calcium-oxalate-type kidney stones[28], and phosphate-type kidney stones[29]. Kidney stones are known for their intense autofluorescence which has even been used for experimental evaluation of human kidney stone fluorescence spectra[30]. Chemical bleaching of renal stones was one approach to reduce fluorescence in Raman spectra at 532 nm laser excitation[31]. Other approaches analyzed human urinary stones by FT-Raman [32,33] and a portable dispersive Raman system [12] both at 1064 nm excitation to suppress unwanted fluorescence background. Raman chemical imaging using a confocal Raman microspectrometer generated maps of the constituents' distribution in a case study of structural analysis of kidney stones [34]. It was concluded that (i) huge autofluorescence background interferes with the detection of low concentrated and poor Raman scatterers and (ii) this analysis is time consuming. The Raman imaging spectrometer described here allow a faster and more sensitive way to map kidney stones due to the larger laser diameter and absence of fluorescence background. Furthermore, the lower confocality of our fiber probe instrument would facilitate mapping of uneven stone surfaces. First experiments in Figure 5 compare the exceptional spectral quality of 1064 nm excited Raman spectra of four kidney stones with 785 nm excited Raman spectra which are dominated by about 10 times more intense fluorescence background in cases #3 and #4 with a darker appearance. The 785 nm Raman spectra were collected with a state-of-the-art instrument (RNX1

Preprints.org (www.preprints.org) | NOT PEER-REVIEWED | Posted: 15 April 2024 doi:10.20944/preprints202404.0864.v1

microprobe, Kaiser Optical System, USA) that was used in a previous study[15]. The better signal-to-noise ratio with the 1064 nm instrument is due to the longer exposure time (5 seconds) and higher laser intensities (400 mW) and enables the assignment of the Ca^{2+} hydrogen phosphate stone (case #1), Ca^{2+} oxalate monohydrate stone (case #2), and cystine stones (case #2 and #4). To avoid detector saturation and laser-induced sample destruction, the exposure time and laser power were reduced to 1 second and 100 mW for the 785 nm instrument, respectively. This clearly demonstrated the benefits 1064 nm Raman spectroscopy, and more data will be collected in the future.

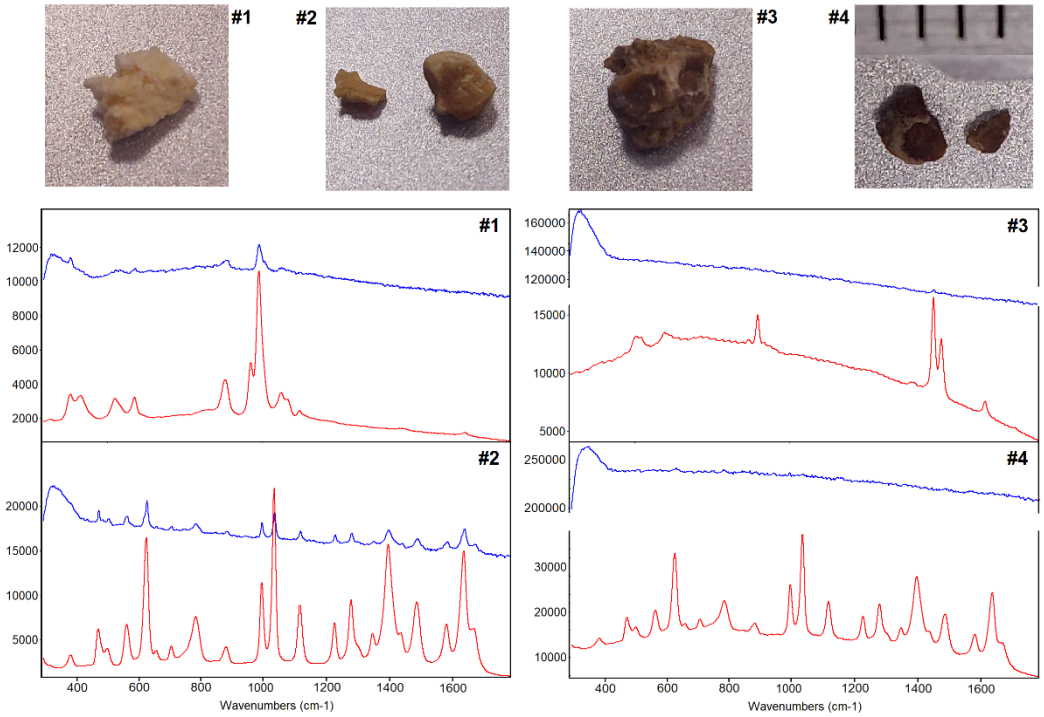

Figure 5. Photomicrographs and Raman spectra of kidney stones at 785 nm (blue traces) and 1064 nm excitation (red traces). Unprocessed spectra are displayed at an appropriate intensity scale for comparison. The scale of a ruler in mm units in #4 is also valid for #1 to #3.

5. Conclusions

A Raman system with 1064 nm excitation laser was coupled to a fiber probe, digital microscope and motorized stage. The near infrared excitation wavelength (λ) enabled penetration down to several hundred micrometers. The detection by a lens with NA 0.3 in combination with a 600 µm fiber core gave poor confocality, but offered extracting volumetric information from deeper tissue layers which partly compensates lower scattering intensity due to the λ^{-4} Rayleigh law. Due to the focus diameter near 200 µm, a high-precision motorized stage was not required and an inexpensive model was selected instead with a large scan range of 200x300 mm. Overall, such a compact and versatile Raman instrument shows great potential for applied sciences, in particular for samples with high fluorescent background.

The performance of the 1064 nm Raman instrument was demonstrated for non-tumor and tumor specimens of resected human bladders. Radical cystectomy is performed in patients with high-grade, muscle-invasive tumor diseases. Due to previous treatments such as endoscopic resection of non-muscle-invasive tumor and photodynamic therapy, necrosis is often present beside lipid-rich, control and tumor tissue. Preprocessing of 1064 nm Raman images by baseline correction, smoothing and normalization followed by processing with KMC and HCA revealed four clusters that were assigned to necrosis, lipid-rich, control and tumor tissue. The findings agreed well with Raman images at 785 nm of these specimens. Deviations between 1064 nm and 785 nm Raman data sets might be due to different sample orientations. Proper correlation with the histopathological gold standard of parallel hematoxylin and eosin stained tissue section is also impaired by different orientations. Resected

 doi:10.20944/preprints202404.0864.v1

tissue can be stained by inks to label the orientation e.g. to assess the tumor margin. However, these inks give intense Raman signals and/or high background that interfere with the spectral fingerprint. The 1064 nm option would be interesting for Raman imaging of intraoperative specimens with ink labels because inks do not contribute to 1064 nm excited Raman spectra. Another interesting urological application of a portable dispersive 1064 nm fiber probe Raman imaging spectrometer is the assessment of kidney stones whose Raman spectra are often affected by intense fluorescence at visible excitation wavelengths. It was shown that the identification of the stone type failed in two cases.

Author Contributions: Conceptualization, J.D.M.B. T.A.S and C.K.; methodology, J.D.M.B. and T.A.S; software, J.D.M.B. and T.A.S; investigation, J.D.M.B.; resources, C.K., J.P., and A.M.; writing—original draft preparation, J.D.M.B and CK.; writing—review and editing, all; supervision, C.K. and J.P.; funding acquisition, C.K and A.M.. All authors have read and agreed to the published version of the manuscript.

Funding: This work has partially been funded by the German Federal Ministry of Education and Research (BMBF) under the project UroMDD (03ZZ0444).

Institutional Review Board Statement: The study was conducted in accordance with the Declara-tion of Helsinki, and approved by the Institutional Ethics Committee) of University of Freiburg (protocol code 592/17 (191723) approved on January 30th 2020) for studies involving humans.

Informed Consent Statement: Informed consent was obtained from all subjects involved in the study.

Data Availability Statement: Raw data will be provided upon request.

Acknowledgments: The authors thank Dr. Peter Bronsert (Faculty of Medicine, University Freiburg, Germany) for support to provide bladder specimens.

Conflicts of Interest: The authors declare no conflict of interest.

References

1. Krafft, C.; Popp, J. Opportunities of optical and spectral technologies in intraoperative histopathology. *Optica* **2023**, *10*, 214-231.
2. Lee, M.; Herrington, C.S.; Ravindra, M.; Sepp, K.; Davies, A.; Hulme, A.N.; Brunton, V.G. Recent advances in the use of stimulated raman scattering in histopathology. *Analyst* **2021**, *146*, 789-802.
3. Krafft, C.; Schie, I.; Meyer, T.; Schmitt, M.; Popp. Developments in spontaneous and coherent raman scattering microscopic imaging for biomedical applications. *Chemical Society Reviews* **2016**, *45*, 1819-1849.
4. Kögler, M.; Heilala, B. Time-gated raman spectroscopy – a review. *Measurement Science and Technology* **2020**, *32*, 012002.
5. Korinth, F.; Schmälzlin, E.; Stiebing, C.; Urrutia, T.; Micheva, G.; Sandin, C.; Müller, A.; Maiwald, M.; Sumpf, B.; Krafft, C., *et al.* Wide field spectral imaging with shifted excitation raman difference spectroscopy using the nod and shuffle technique. *Sensors* **2020**, *20*, 6723.
6. Korinth, F.; Shaik, T.A.; Popp, J.; Krafft, C. Assessment of shifted excitation raman difference spectroscopy in highly fluorescent biological samples. *Analyst* **2021**, *146*, 6760-6767.
7. Kozik, A.; Pavlova, M.; Petrov, I.; Bychkov, V.; Kim, L.; Dorozhko, E.; Cheng, C.; Rodriguez, R.D.; Sheremet, E. A review of surface-enhanced raman spectroscopy in pathological processes. *Analytica Chimica Acta* **2021**, *1187*, 338978.
8. Langer, J.; Jimenez de Aberasturi, D.; Aizpurua, J.; Alvarez-Puebla, R.A.; Auguié, B.; Baumberg, J.J.; Bazan, G.C.; Bell, S.E.; Boisen, A.; Brolo, A.G. Present and future of surface-enhanced raman scattering. *ACS nano* **2019**, *14*, 28-117.
9. Guo, S.; Popp, J.; Bocklitz, T. Chemometric analysis in raman spectroscopy from experimental design to machine learning–based modeling. *Nature Protocols* **2021**, *16*, 5426-5459.
10. Schrader, B.; Dippel, B.; Fendel, S.; Keller, S.; Löchte, T.; Riedl, M.; Schulte, R.; Tatsch, E. Nir ft raman spectroscopy—a new tool in medical diagnostics. *Journal of Molecular Structure* **1997**, *408-409*, 23-31.
11. Chao, K.; Dhakal, S.; Qin, J.; Kim, M.; Peng, Y. A 1064 nm dispersive raman spectral imaging system for food safety and quality evaluation. *Applied Sciences* **2018**, *8*, 431.
12. Zhu, W.; Sun, Z.; Ye, L.; Zhang, X.; Xing, Y.; Zhu, Q.; Yang, F.; Jiang, G.; Chen, Z.; Chen, K., *et al.* Preliminary assessment of a portable raman spectroscopy system for post-operative urinary stone analysis. *World Journal of Urology* **2022**, *40*, 229-235.
13. Worldwide cancer data. https://www.wcrf.org/cancer-trends/worldwide-cancer-data (12.01.2024),
14. Lenis, A.T.; Lec, P.M.; Chamie, K. Bladder cancer: A review. *JAMA* **2020**, *324*, 1980-1991.

 doi:10.20944/preprints202404.0864.v1

15. Krafft, C.; Popp, J.; Bronsert, P.; Miernik, A. Raman spectroscopic imaging of human bladder resectates towards intraoperative cancer assessment. *Cancers* **2023**, *15*, 2162.
16. Cordero, E.; Rüger, J.; Marti, D.; Mondol, A.S.; Hasselager, T.; Mogensen, K.; Hermann, G.G.; Popp, J.; Schie, I.W. Bladder tissue characterization using probe-based raman spectroscopy: Evaluation of tissue heterogeneity and influence on the model prediction. *Journal of Biophotonics* **2020**, *13*, e201960025.
17. Yang, M.; Wang, J.; Quan, S.; Xu, Q. High-precision bladder cancer diagnosis method: 2d raman spectrum figures based on maintenance technology combined with automatic weighted feature fusion network. *Analytica Chimica Acta* **2023**, *1282*, 341908.
18. Liu, Y.; Ye, F.; Yang, C.; Jiang, H. Use of in vivo raman spectroscopy and cryoablation for diagnosis and treatment of bladder cancer. *Spectrochimica Acta Part A: Molecular and Biomolecular Spectroscopy* **2024**, *308*, 123707.
19. Munoz-Bolanos, J.D.; Shaik, T.A.; Popp, J.; Krafft, C. *Hyperspectral package for spectroscopists (spectramap)*, Available online: https://pypi.org/project/spectramap/ (accessed on January 14, 2024). 2021.
20. Zhang, Z.-M.; Chen, S.; Liang, Y.-Z. Baseline correction using adaptive iteratively reweighted penalized least squares. *Analyst* **2010**, *135*, 1138-1146.
21. Schafer, R.W. What is a savitzky-golay filter? [lecture notes]. *IEEE Signal Processing Magazine* **2011**, *28*, 111-117.
22. Steller, W.; Einenkel, J.; Horn, L.C.; Braumann, U.D.; Binder, H.; Salzer, R.; Krafft, C. Delimitation of squamous cell cervical carcinoma using infrared microspectroscopic imaging. *Anal Bioanal Chem* **2006**, *384*, 145-154.
23. Krafft, C.; Alipour Didehroshan, M.; Recknagel, P.; Miljkovic, M.; Bauer, M.; Popp, J. Crisp and soft algorithms visualizes cell nuclei in raman images of liver tissue sections. *Vib. Spectrosc.* **2011**, *55*, 90-100.
24. Delrue, C.; Speeckaert, M.M. The potential applications of raman spectroscopy in kidney diseases. *Journal of Personalized Medicine* **2022**, *12*, 1644.
25. Carmona, P.; Bellanato, J.; Escolar, E. Infrared and raman spectroscopy of urinary calculi: A review. *Biospectroscopy* **1997**, *3*, 331-346.
26. Cui, X.; Zhao, Z.; Zhang, G.; Chen, S.; Zhao, Y.; Lu, J. Analysis and classification of kidney stones based on raman spectroscopy. *Biomed. Opt. Express* **2018**, *9*, 4175-4183.
27. Kodati, V.R.; Tu, A.T. Raman spectroscopic identification of cystine-type kidney stone. *Applied Spectroscopy* **1990**, *44*, 837-839.
28. Kodati, V.R.; Tomasi, G.E.; Turumin, J.L.; Tu, A.T. Raman spectroscopic identification of calcium-oxalate-type kidney stone. *Applied Spectroscopy* **1990**, *44*, 1408-1411.
29. Kodati, V.R.; Tomasi, G.E.; Turumin, J.L.; Tu, A.T. Raman spectroscopic identification of phosphate-type kidney stones. *Applied Spectroscopy* **1991**, *45*, 581-583.
30. Schütz, J.; Miernik, A.; Brandenburg, A.; Schlager, D. Experimental evaluation of human kidney stone spectra for intraoperative stone-tissue-instrument analysis using autofluorescence. *Journal of Urology* **2019**, *201*, 182-188.
31. Kocademir, M.; Kumru, M.; Gölcük, K.; Suarez-Ibarrola, R.; Miernik, A. Fluorescence reduction in raman spectroscopy by chemical bleaching on renal stones. *Journal of Applied Spectroscopy* **2020**, *87*, 282-288.
32. Selvaraju, R.; Raja, A.; Thiruppathi, G. Ft-raman spectral analysis of human urinary stones. *Spectrochimica Acta Part A: Molecular and Biomolecular Spectroscopy* **2012**, *99*, 205-210.
33. Tonannavar, J.; Deshpande, G.; Yenagi, J.; Patil, S.B.; Patil, N.A.; Mulimani, B.G. Identification of mineral compositions in some renal calculi by ft raman and ir spectral analysis. *Spectrochimica Acta Part A: Molecular and Biomolecular Spectroscopy* **2016**, *154*, 20-26.
34. Castiglione, V.; Sacré, P.-Y.; Cavalier, E.; Hubert, P.; Gadisseur, R.; Ziemons, E. Raman chemical imaging, a new tool in kidney stone structure analysis: Case-study and comparison to fourier transform infrared spectroscopy. *PLOS ONE* **2018**, *13*, e0201460.